Advanced Mechanical Design, University of Rochester
Final Design Report
Spring 2026

THE DESIGN AND OPTIMIZATION OF A SMALL-SCALE CASSEGRAIN TELESCOPE

Mahir Abbaker **Izzy Doty** **Morgan Edstrom** **Evan Thomas**

ABSTRACT

The aim of this project was to design, iterate, assemble, and test a Cassegrain telescope, satellite that can image. The assembly consists of four major subsystems: the Primary Mirror Mount (PMM), the Secondary Mirror Mount (SMM), the struts, and the camera mount/imaging system. All main structural components were fabricated and simulated as Aluminum 6061 (Al 6061) and connected through steel ball joints and neodymium magnets that were glued internally in the struts. During the design phase, the focus was on evaluating the PMM, refining the interface connections, and developing an effective adjustment mechanism to achieve precise alignment. After initial iterations of all structural components were created, to optimize and lightweight the satellite, simulations were developed.

Structural analysis was performed in NX, specifically with the Simcenter NASTRAN structural solver. The main methods of analysis at the subassembly and assembly level were modal analyses (SOL 103), thermal expansion in the linear static case (SOL 101), non-linear quasi-static gravity loading (SOL 106), and linear buckling (SOL 105). All strength specifications were met with positive margins of safety of 2.60 and 18.3 margins for lateral and axial cases respectively at yield. At the ultimate failure margins of safety were positive margins of 2.37 and 17 as well. Thermal deformation under the specified soak temperature produces a maximum deflection of 1.02E-3 inches, leaving 73.85% of the optical tolerance available. All parts successfully reduced their mass by at least 10% from their initial iterations, while simultaneously maintaining deflection within specification. The main failure to meet specifications was for the modal analysis. At a subassembly level, all subassemblies met the 180 Hz requirement, except for the SMM. At the larger, assembly level the first significant mode of the system was found to be 112.30 Hz. This was driven by the low lateral stiffness of the SMM as well as the thickness of the tubes. Future work can iterate on a fundamental redesign of the SMM to address the modal deficiency, explicit modeling of all connections (bolt preloads/magnetic preload) and interfaces, as well as further optimization of the geometry of the entire model to maximize weight reduction while balancing strength and stiffness as well as reducing part count as there were 1.89% more parts than last year's iteration, failing the specification.

PROBLEM DEFINITION

Satellites are highly complex and resource intensive systems that deliver essential data and images from space requiring significant time, cost and technical expertise to design and maintain. Developing a small-scale version of these systems provides more accessible and cost-effective platform methods to study performance and test improvements.

REQUIREMENTS, SPECIFICATIONS, DELIVERABLES

Deliverables:

The following design presents four subsystems that compose the entire satellite. The components include the struts, camera mount, Primary Mirror Mount, and Secondary Mirror Mount. The final product present is evaluated to have a functional image capturing system and test data that is up to specifications.

Requirements:

The primary requirement for this optical device is that the device is cost-effective and capable of imaging. In addition, the design must imitate a Cassegrain design method.

Specifications

Value & Units	Description & Method of Evaluation
18.00 G	The optical structural assembly (OSA) shall maintain positive Margin of Safety (MoS) > 0.0 under Quasi-Static Limit Loads of Lateral. Method of evaluation: Perform simulation and a tensile test using the MTS machine. Apply strain gauges to check for permanent deformation. Inspect for cracks or visible failure.
180.00 Hz	The fixed-base fundamental natural frequencies of the stowed optical assembly. Method of evaluation: Simulation and perform an impact hammer test using accelerometers and a DAQ system to identify resonance peaks.
10.00 %	Reduction of part count to simplify assembly. Method of evaluation: Compare the part count with the previous year's design iteration.
10.00 %	Achieve a 10% reduction in total structural weight (including lenses) from the initial CAD design while maintaining a factor of safety of 1.25 against yield. Method of evaluation: Compare the final assembly weight on a digital scale with initial NX mass-property estimates.
0.00039 in	Resolution of secondary mirror adjustment. Method of evaluation: Set up the optics and image a sample target located 72 inches away.
0.0039 in	The optical assembly shall maintain focus over an operational soak temperature of 122°F ±3.6°F for 60 minutes. Thermal expansion (CTE) induced defocus shall not exceed. Method of evaluation: Simulate the assembly and place it in an oven; use markers to detect any lens displacement.
12 G	The optical structural assembly (OSA) shall maintain a positive Margin of Safety (MoS) > 0.0 under Quasi-Static Limit Loads of 12G (Axial). Method of evaluation: Perform simulations and verify simulations through tests.
1.5 FS	Factor of safety against ultimate.
1.25 FS	Factor of safety against yield.
14 %	Reduction of obstruction of the primary lens.

CONCEPTS

Primary Mirror Mount Selection:

The function of the Primary Mirror Mount (PMM) is to provide enough stiffness and strength to the entire satellite so that the maximum deflection of any part is less than 0.003 inches. This is because precisely optical mirrors require accurate focus. The PMM was also designed so that it could interface with both the struts to the Secondary Mirror Mount as well as the camera mount. This meant that any design choice of the PMM had to have a surface area along a 10-inch diameter and a 5-inch diameter, for the struts to the SMM and the camera mount. The concept initially began as a hoop design that spanned both diameters. Due to manufacturability constraints, the PMM then became a hexagon formed from six different trapezoidal bases, while also maintaining the diameters for the struts interface as shown in Figure 1. After talking to the manufacturing technical staff, it was determined that six pieces would be more difficult to manufacture than a single hexagonal piece, confirmed by the Pugh Matrix and became the final design choice.

TABLE 1: Pugh Matrix Determining PMM Final Design

Criteria	Hoop Base	6 Piece Trapezoidal Base	Single Hexagon Base
Manufacturability	-	+	+
Material Used	+	-	-
Ease of Assembly	+	-	+
Ability to be mounted to tripod	-	+	+
Total	0	0	2

Attachment Mechanism:

Precise optical systems must be held together in a robust and repeatable manner. To accomplish this for the satellite, some areas of design that were paid special consideration to be the appearance of slop in the mechanism, ease of assembly, manufacturability, and cost. The attachment mechanism chosen must be adaptable such that it can be applied to both the connections between struts and base plates as well as the connection between camera and the camera mount. After careful consideration of three attachment mechanism options, the optimal choice was determined to be magnetic ball joints.

When examining mechanical ball joints as an option (figure 3), a prominent concern lies in the slop between the ball and socket without the presence of any biasing forces. This can be mitigated with the additional installation of a spring or flexible band; however, for the sake of the Pugh Matrix below, the additional parts needed to counter the problem of slop are not included. As a counter design which does not require consideration of slop, wire flexure attachments were examined (figure 4). Unfortunately, despite wire flexures allowing for small bending deformation and no axial deformation, the design we considered required several parts which negatively affected its ease of assembly and manufacturability score. As a result of the shortfalls present in the previous two design options, a third option of a magnetic ball joint connection was considered (see figure 5). The magnetic connection prevented any slop present in the joint, while the ball collection allowed for the bending movement required for small adjustments in strut length. Due to this design choice requiring only two parts as well as a simple assembly, it scored highest in the Pugh matrix and was consequently chosen in the final design.

TABLE 2: Pugh Matrix Determining Interface Connection

Criteria	Mechanical Ball Joint	Wire Flexure	Ball Joint (magnetic)
Slop	-	+	+
Manufacturability	+	-	+
Ease of Assembly	-	-	+
Cost	-	+	+
Total	1	2	4

Adjustment Method Selection:

To ensure the accuracy, alignment, and focus of a sensitive optical system, an adjustment method must be carefully selected. The method in question must provide sufficient resolution and precision for the optical alignment while reducing the amount of slop, while still being manufacturable, and easy to adjust. Three systems were evaluated: a differential screw system integrated into the struts, a wedge piece sitting at the interface points, and a spring bias system also sitting at major interface points. It was determined that the wedge system was the most effective choice due to its ability to reduce slop as well as giving adequate precision to the overall optical system, with the addition of a spring to help decrease slop.

TABLE 3: Pugh Matrix Determining Final Adjustment Method

Criteria	Differential Screw	Wedge Piece	Spring Bias
Slop	0	+	++
Manufacturability	0	+	+
Ease of Assembly	0	+	-
Resolution	0	+	-
Total	0	4	1

MECHANICAL ANALYSIS

Tolerance Analysis:

The alignment of the optics and camera is the primary metric of successful operation of this telescope. It should be expected that the mechanical tolerances of each subsystem must be deliberately and precisely calculated.

As previously outlined, the adjustment mechanism for the entire telescope depends on a set of twelve wedges that can be raised or lowered on one end according to the rotation of a thumbscrew. Since the thread pitch of each thumb screw is 1/32”, every full rotation of the thumbscrew raises the back end by 1/32”. The distance between the screw base and the rotation point of each wedge adjustment block is 2” and the distance between the base of the strut and the rotation point is 1” (as seen in Figure 6). As such, for every full turn of the thumbscrew, the strut is raised upward by 15.6 thousandths of an inch. Since each thumbscrew has 20 full turns possible, each strut can be moved 0.312” upwards from the base height. Any tolerance permitted in machining the primary mirror mount, the adjustment wedges, the struts, and the secondary mirror mount must add up to less than 0.212” to ensure 100 thousandths of adjustment is still possible in the +Z direction.

Further, assuming 100 thousandths of adjustment in the +Z direction, we can determine the maximum angular adjustment possible in the secondary mirror mount to be 1.788 degrees. In the camera mount base plate, the maximum angular adjustment is 2.1 degrees.

Fatigue Analysis:

Whilst the primary plate carries a high stiffness, which is required for gradual optical alignments, to prevent yield during launch and thermal expansion cycles in space, it must also have high cycle fatigue. When faced with intense acceleration and G-forces during launch, the satellite is subjected to strong vibrations. This loading excitement creates localized points of fatigue failures. This discussion presents a complete fatigue analysis assessment methodology by comparing the ultimate strength of the 2 metals.

Noting the ultimate tensile strength of steel to be 310 MPa, the yield strength of 276 MPa, and a fatigue strength of 96.5 MPa for 5E8 cycles. Unlike most other alloys, 6061 does not exhibit a true endurance limit, allowing fatigue and strength to degrade beyond 10E7 cycles. Therefore, the ultimate tensile strength is recognized as a value of 5E8 cycles which is a conservative bond that holds consistent with MMPDS5-01 [9].

Conclusive fatigue analysis considers stress contributions at critical nodes noted by an NX simulation using the Solution 103 real eigenvalue identification. Whilst alternating stresses are gathered from random vibration noted by the Solution 111 frequency responses on a PSD table, analyzing the root mean square (RMS) von mises stresses at the critical locations. Per the [MSFC-STD-3679], the 3-sigma peak envelope is used to bound stress amplitudes.

The mean stress is the baseline stress throughout vibrational events. It contributes to the fastener preloads at the adjustment wedge constraints and the mirror mounting interfaces, and stress induced by CTE mismatches between the Al 6061 and adjacent structures. Both of which are determined from the SOL 101 static solvers evaluated at critical notes. With tensile mean stresses being most detrimental for fatigue life since it holds crack faces open and propagates stresses along cracks. Since analysis results show the stress faced by the optical site is less than the ultimate stress of steel at 5E8 cycles. This satellite would thus pass fatigue and be able to operate at load of 10 Gs.

Camera Mount:

The camera mount assembly was analyzed for deformation under the gravitational load of the camera and mount weight. Additionally, by repeating this analysis and removing weight from the mount between each iteration, it was possible to accomplish a 37% reduction from the original mass. Lightweighting was performed by removing radially symmetric sections of material from the base plate that did not interfere with any critical components in the assembly. The final maximum deformation of the optimized structure was 20 thousandths of an inch. This is well below the total adjustment capabilities of the camera struts (312 thousandths). The 3 iterations of lightweighting are depicted in figure 17.

Torque Analysis:

The interface of the Primary Mirror Mount (PMM) and the blocks to mount the optics requires precise balance and stiffness so that the mirrors do not misalign. The three mounting blocks were positioned around the primary mirror and fastened down using a 10-24 Black Oxide fastener. The torque required to ensure that they are properly secured but still removeable is calculated using material quantities of the fastener and equations presented in Shigley's Mechanical Engineering Design book [9]. The preload was calculated from equation 1 to be 1.575E03 lbf, such that the tensile stress area (At) was 0.0175 inches, and the proof strength (Sp) was 120 kpsi. Using this value, as well as a diameter (d) of .19 in, and a bolt condition coefficient (K) of 0.20, the final torque needed to secure the fastener from equation 2 was determined to be 59.85 psi.

$$F_i = 0.75 \cdot A_t \cdot S_p \tag{2}$$

$$T = K \cdot F_i \cdot d \tag{3}$$

Overall Material Selection:

The primary structural material selected for the optical satellite is Aluminum 6061 (Al 6061). This alloy was selected based on three primary criteria: cost, accessibility, and its material properties. Al 6061 exhibits a high Young's Modulus 68.9E3 MPa an ultimate tensile strength of 275.95 MPa, a yield strength of 241.7 MPa, and a density of 2.70 g/cm³, [2] providing a strength-to-weight ratio suitable for most if not all structural components of the satellite. Aluminum alloys are among the most widely used metals in spacecraft manufacturing, offering high strength-to-weight ratios, high ductility, and ease of machining, [3] which created a solid basis of material selection to design around. Furthermore, Al 6061 is widely available through most industrial suppliers and the Mechanical Engineering department's favored supplier (McMaster) ensuring reduced lead times and procurement costs relative to alternative materials such as titanium alloys or carbon fiber reinforced polymers.

Neodymium Iron Boron (NdFeB) magnets were selected under the same criteria as the aluminum, with the addition of magnetic force capacity as a primary determining factor. The magnet geometry was constrained by the inner diameter of the struts, determined to be 0.555 in., limiting the selection to disk or cylindrical magnet forms with a maximum diameter of 0.500" given standard available sizes through the vendor, K&J Magnetics. In consideration of the uncertainty associated with the interface point loading conditions, a higher strength magnet was favored to provide an additional level of safety in the magnetic connection, due to the uncertainty of weight of the final structure during the final design phase. The selected magnet provides a holding force of 15.1 lbf, with a final geometry of 0.500" diameter and of 0.625" length.

At each magnet interface point, the presence of a ferromagnetic material was required to maintain the connection between components. Multipurpose low-carbon steel was selected as the primary material for all inter`face balls based on its ferromagnetic compatibility, mechanical properties, accessibility, and cost. As a ferromagnetic material, low-carbon steel can attach to the neodymium magnets, with a reliable magnetic connection at the interfaces of the model. A critical design requirement at the interface was the need for the satellite structure to remain exactly constrained at the connection points between the interface balls and the adjustor plates/struts. This necessitated tight dimensional tolerances on the ball geometry, as any deviation in sphericity or diameter would introduce slop at the interface, compromising the kinematic constraint and degrading the alignment of the system. The selected balls (McMaster-Carr P/N 9615K59) are ¾" diameter, case hardened to Rockwell C60 (extra hard), with a diameter tolerance of +/- 0.005" providing the dimensional consistency required without finishing operations to save manufacturing time as a team. The case-hardened surface additionally provides wear resistance at the interface points under repeated contact loading during assembly, adjustment, and operation. The contact with the magnets if carelessly applied can cause them to shatter, rendering them inoperable, so having an interface being able to handle that impact was an important consideration.

Spring Size:

Assembling current models for the optical satellite required interfaces that mount the primary mirror mount to both the secondary and camera mounts. To connect the struts designated to each subsystem, the interfaces are mounted to one another with kinematic mounts. In addition, to ensure such mounts are not over constrained and don't decouple, they are connected using 2 hooked extension springs that lie in parallel to one another. These configurations procure an equivalent resistance of 20.8 psi and in turn a maximum load capacity of 11.64 lbf. These springs provide force to counteract the preload of the top-down assembly consisting of the secondary mirror mount and the struts, which are 1.137 lbf. To allow for the mount to hold the springs must have an initial static extension of at least 0.0555 inches. This low displacement factor ensures that proper stabilization of the interfaces without the need to reach the maximum extension rating of the springs, which is 1.163 inches. Ensuring that the springs will be able to preserve strength without facing strong fatigue and deformation in springs.

In addition to providing substantial force to bear minimum static loads, the following springs provide a safety factor of 10.24, which provides insurance against both static and dynamic loads that are applied during launch. This ensures that the interfaces will not slip or decouple due to either static preload conditions during launch. Whilst also accounting for the tolerances of 10%, at the worst cast minimum stiffness drops to 18.72 psi only increases the minimum static extension to 0.061 inches. This is an acceptable range to fall to as it would still provide a stiff robust connection between the interfaces.

FEA Analysis of the PMM:

The function of the primary mirror mount is to provide enough stiffness to the entire satellite so that the maximum deflection of any part is less than 0.003 inches. Because of this requirement, the PMM was manufactured from a 0.625-inch thick piece of aluminum, which, including the primary mirror optic, had an initial mass of 10.369 lbm with a deflection significantly lower than the maximum. Therefore, to increase the strength to weight, mass was taken out of the PMM and to confirm that it maintained enough stiffness to support both the camera mount and the secondary mirror mount, a structural FEA was performed. The FEA was set up so that the camera mount and the SMM were represented by an individual center of mass. The PMM itself was created using a Tet10 mesh of .3 inches, with Aluminum 6061 assigned material. The PMM was constrained along a 4-inch central region on the bottom face to represent its mounting interface with the tripod. With each iteration of lightweighting, the maximum deflection of the system as well as the mass of the PMM and optic was organized in Table 4. Detailed FEA results and iteration geometry are provided in Appendix B

Table 4: Optimization of the PMM mass

Iteration	Max Deflection [in]	Mass of PPM + Optic [lbm]
A	8.460E-04	10.369
B	9.178E-04	8.975
C	1.234E-03	7.1575
D	2.534E-03	5.3773

FEA Analysis of the Struts:

The final strut geometry for the struts is an outer diameter (OD) of .625", and an inner diameter (ID) of .555", which results in a thickness of .035". The manufacturing guided the design and analysis for both struts. For the longer strut 0.375" through-holes alternating every 90° along the strut axis at 0.5" spacing, they were modeled. For the smaller struts, the same pattern is present but reduced to .25" to account for the smaller geometry. Buckling analysis of the final strut iteration (connecting the PMM and SMM) yielded a Factor of Safety of 274.74 psi for the first buckling mode under 1 lbf axially in the –Z direction, confirming structural stability under the applied loading and allowing for any uncertainty in loading for the PMM or SMM. The struts were constrained with the boundary conditions of SPC 12 at the top and SPC 1236 at the bottom. With these assumptions, extra stiffness was added to the structure as in reality; this is not how the struts are constrained. However, the results indicate an overdesigned structure in buckling. This can be seen from the FoS that is obtained divided by the 1.25 outlined in the specifications then subtract 1. This obtains a result of more than +200. The mass reduction recorded by NX was 0.1186 lbm to 0.0942 lbm, representing a 20.6% reduction in mass falling within specifications. (Figure 12) With such a large margin of safe A midsurface was used as idealized geometry when creating the mesh with a CQUAD4 with a mesh size of .15" and a material assumption of Al 6061. RBE2s were used at either end of the tube using the point to edge method for the internal diameter to the center of the tube. Theoretically, the internal magnet mass should correspond to an RBE3 connection at the boundary conditions. However, the axial load case is compressive along the axis of the tube rather than locally distributed load at the glue connection. The mass of the magnet is negligible in the larger buckling response of the tube. Additionally, the high factors of safety under 1 lbf loading should account for any uncertainty introduced by the magnet at larger loading conditions and its connection internal to the tube. For a future, more accurate model, an RBE3 connection can be considered with a 0D element representing the magnet force but should account for the reduction in magnetic force as distance increases from the opening of the tube. Again, the constraints used were a SPC 12 at the top RBE2 connection where the 1 lb. force was applied and an SPC 1236 at the bottom RBE2 connection. Additional constraints for either SPC add artificial stiffness to the model, in turn creating inaccuracies in both the buckling and modal analyses.

For the shorter struts connecting the PMM to the camera mount, its FEA results indicate a theoretical FOS of 1.079E4 psi in the first buckling mode, which makes sense for a short, stiff tube section. The mass reduction achieved was 0.0182 lbm to 0.0151 lbm, representing a 17.0% reduction in mass, falling within mass specifications. (Figure 15) The maximum Von Mises stress is 2.362E6 psi. It used another midsurface as idealized geometry, the same material assumptions, constraints, loads, and RBE2 connections. The only difference present was the mesh size of .125". This result should be treated as realistic without the need for a convergence study due to an extremely high margin of safety. This can be obtained from the FoS divided by the 1.25 outlined in the specifications then subtract 1. This obtains a result of more than +8,000.

The modal and thermal analyses followed the same SPC and RBE2 assumptions at the boundary conditions. The 106 solution that would include the G-load of the struts was deemed unnecessary as this needs the context of the entire assembly to yield accurate results. The important results on the subassembly level are the buckling and modal results. The modal analysis in isolation meets specifications under these assumptions for longer struts. The SOL103 analyses yielded a first mode result of 212.95 Hz and a displacement of 101.09" as well as a maximum Von Mises element-nodal stress of 1.478E7 psi for the longer struts. (Figure 14) The shorter struts being significantly smaller one should expect to see larger natural frequency. This is matched by the 103 results, with a modal result of 3.918E3 Hz to get a displacement of 204.44 inches, at a mesh size of .0833" (Figure 16). It is unrealistic that this would occur in reality. The larger struts will be the determiner of failure modally before this occurs. The critique of the assumptions made, with the knowledge of the larger assembly results, artificially raises the stiffness of the strut leading to a higher natural frequency, in comparison to how it would react in the larger assembly.

FEA of the Assembly:

When approaching the assembly analysis, the key considerations maintained throughout the process were mixing computational intensity with accuracy of results. Generally, a conservative approach was taken when running and creating the analysis of the system. A fine mesh solid model with all connections maintained, and no assumptions made can create runtimes of hours to solve, with no guarantee of an accurate or converging model. Several modeling assumptions were made when creating the FEA of the entire assembly.

All bolted connections, dowel pins, and ball interfaces were modeled as rigid connections. The dowel pin and bolt connections were modeled using coincident glue mesh mating conditions. This was appropriate for both types of interfaces as both connections share the same geometry on the SMM. In addition, their position allowed mesh nodes at the specific interfaces to coincident properly for this mating condition. The glue mesh mating constrains all DOF at the mating surface correctly replicating the fastener/dowels that should transfer load rigidly between the mated geometry with no slip at the interface. While this approach does add artificial stiffness into the local connection and around the geometry because of the assumption that there is a rigid bond present, for the sake of analysis it was deemed necessary as a conservative method during the analysis. It should represent the upper bound for the interface stiffness' and make sure that load was transferred without compliance at the interface. Similarly, each interface point from the struts to the spheres at the camera mount or PMM were modeled using RBE2 elements with an edge-to-edge recipe. This creates a fully rigid constraint between the independent and dependent nodes, removing all translational DOF. This was deemed appropriate and like the glue coincident, a conservative estimate of how stiff the system would be and overestimating the load that would go through the system. If the structure survived under stricter conditions, it could be assumed that the structure could perform better where some compliance exists in the system. If the magnets were considered in the analysis explicitly, each magnet would be meshed as a solid component, with the correct material properties and a compressive load being part of the pre-load conditions in the simulation. This would allow the pre-load to travel the proper load path in the system. However, as stated in the strut analysis, the magnet was deemed unnecessary. The artificial stiffness created by the RBE2 assumption creates the stiffest possible iteration, and the inclusion of the magnet should be considered a subcomponent analysis rather than the assembly level FEM.

Mesh size was approached from the perspective of computational efficiency. All struts and interfaces were meshed with a CTETRA(10) at a size of .3". All mounts were also meshed with a CTETRA(10), but with a larger size of .7". The reason that a CTETRA(10) mesh was selected over a CTET4 was to ensure that rather than in the interface points, the structural elements did not have any artificial stiffness. The selection of the CTETRA(10) was a choice made to ensure that during modal results, one of the key specifications was accurate when simulated. The CTETRA(10) in theory should allow for more compliance when being and better capturing the deformation that should occur. This is notable when comparing the artificial stiffness knowingly added at the interfaces. That stiffness was introduced as a conservative assumption where load transfer will occur. Adding artificial stiffness to structural elements would create inaccuracies rather than a conservative assumption. With this in mind, the size of the meshes was also intentional. The PMM and Camera Mount being the stiffest and less critically loaded components and could be larger meshes.

For the simulation, it was assumed that the only fixed part of the assembly would be one plane of the PMM matching what would be the physical assembly on its mount (Figure 32). This portion of the assembly was again given a fixed constraint to match the physical model. Four simulations were done, one SOL 103 analysis, a SOL 101 for thermal expansion analysis, and two SOL 106 analyses for the system under the specified gravity load. It should be noted that the the 103 analysis did not include this fixed constraint as initial simulation results were being deflated.

The results of the general analysis indicate a generally accurate model, but a failure to meet the modal specification with the assumptions being made. The first significant mode is found to be 112.30 Hz in the 7th mode under the stiffest conditions. While each individual component meets the modal requirement,, the SMM does not. This may have been the cause of the severe displacement of the SMM to cause the entire system to be displaced along with it (Figure 21). Much of the deformation appears to be torsional rather than bending. This observation is consistent with the FoS observed in the individual struts. Several of the modeling decisions made could have artificially depressed the modal results, and the addition of the magnet pre-load would have stiffened the structure, and the CTETRA(10) assumption may have over-predicted the flexibility of the system. There is the additional fact that with the adjustor plates with springs, full kinematic mount of the camera, and preload of the bolts/dowels/being unmodeled, that should introduce more stiffness into the structure inherently with more mass in the system, but could possibly introduce compliance if defined correctly. If the springs of the kinematic mounts were introduced, a CELAS1 should be used so that the stiffness can be controlled at the interface; however, this would introduce more compliance into the system, ultimately making it less stiff. It is also important to note that the results on a physical level make some sense. Kinematically, the system should be driven by the interface stiffness rather than material stiffness as all subassemblies pass the modal requirement except the SMM at 124.4 Hz (Figure 19). The SMM is incredibly light. Through the solid properties check tool in NX, the mass of the SMM is ~.4215 lbf compared to the PMM of ~5 pounds. One would expect deformation to occur around the struts and/or the SMM because of this. The SMM itself, if redesigned to account for this displacement of 31.94", would need to increase stiffness by increasing the mass or approach the SMM as singular part or close to a singular part as possible, centralizing mass. The struts themselves can also be at fault. The lightweighting, although deemed to have passed metrics for analysis at the subassembly level, may have created additional causes for failure to meet the modal specification. By introducing this reduction in mass, it also in turn reduces structural stiffness as seen contributing to the deformation in Figure 21. It should also be noted that the radius of the SMM should also be decreased. A possible solution is increasing the angle between the struts and the SMM. It should in turn increase the stiffness of the structure, although it should be noted that obstruction of the optic will occur. Overall, the key takeaway from this analysis is that even in the theoretical stiffest scenario, modal results do not meet specifications and need to be accounted for in future iterations with additional simulation considerations.

The thermal results as well as the G-load more than exceed expectations (Figures 24 and 25). The self-loading during the analysis, and the lightweighting at the subassembly level created this result. The result of the thermal analysis is a deformation of 1.02E-3" under the specified temperature, giving 73.85% of the tolerance still available after loading, putting the result well within specifications. The same goes for the 106 solutions' results. The G-loads were done separately as if the assembly could handle a lateral G-load larger than the axial. There should be no reason to do them simultaneously. The maximum Von Mises stress value was found to be 6915.04 psi, at the edge of the RBE2 connection from the strut to the SMM, which seems to be artifacts from the initial analysis, however even at the maximum it has a positive MoS. Similarly, the axial G-load gives a maximum Von Mises result of 1287.2 psi. With NX's material properties library [2], Al 6061's yield strength at the operating temperature of 122 degrees Fahrenheit is 215,116 kPa or 31,120 psi. With Equation 4, obtaining the MoS for both cases (laterally and axially respectively) to be +2.6 and +18.3 margins. For the MoS against ultimate following the same formula with the ultimate strength at 122 degrees Fahrenheit being 35,000 psi. With 1.5 as the factor of safety for the ultimate condition, a MoS of +2.37 for the lateral case and +17 for the axial case is obtained.

$$MoS = \frac{\frac{F_{yield}}{FoS}}{\sigma_{max}} - 1 \ (\#4)$$

There was a failure to meet specifications on the reduction of part count. Last year's assembly contained 127 parts in the final assembly. The final assembly file contains 144, when accounting for suppression of parts that should not be present in the file. That accounts for a 1.89% increase in part count. Future iterations should focus on solid models, reducing complexity when possible.

Fundamental Mechanical Analysis:

For the system, the mechanical deviation that was accounted for to reach the deliverable demands to light weight and maximize the strength to weight of the assembly required a visualization of the secondary mirror mount as a cantilever beam. Noting the increase in the moment arm the farther the forces are applied from the beam. To maximize the strength to weight ration material was removed in a pattern-based hole configuration along the span of the mirror mount arms. With the fundamental assumption that material near the neutral axis provides considerably less bringing relative to its weight [9]. The holes are patterned along the neutral axis where shear stress is present rather than stress. This would guarantee that each hole that is introduced allows for passable stress concentrations. Provided the stress located on the arms with the holes provide a maximum principal stress of 289 psi when subjected to 18 Gs' of force as noted in Figure 10. Unlike a beam without holes which displayed a max principal stress of just 266.40 psi.

MANUFACTURING

Table 5: Build Costs

	Cost ($)
Hardware	601.75
Purchased Shop Time	3,000
Team Manufacturing Time ($100/hr)	4,600

Total	8,201.75

`

Table 6: Development Time

	Hours
Morgan Edstrom	86.25
Izzy Doty	24.50
Evan Thomas	66.25
Mahir Abbaker	40.2
Total Hours	217.2
Total Cost for Development in $ ($100/hr)	$21,720.00

Total build cost comes to $21,720.00 in addition to the overall total development of $8,201.75. This brings the total for the satellite project to $29,921.75.

A significant portion of the project cost could have been reduced, as many key components were outsourced to Bill Mildenberger due to time constraints. This included the fabrication of the Primary and Secondary Mirror Mounts, camera plate, and the strut lightweighting features. Sam Kreigsman provided essential support to our in-house manufacturing efforts, assisting with part fabrication and preparing stock material for the wedge adjustment components. Professor Muir also played a key role throughout the process, offering guidance and hands-on support in both the fabrication and assembly of components.

If the satellite system were to be scaled to 1000 systems, both the lightweighting strategies and assembly production would need to be reevaluated to improve efficiency and reduce manufacturing time. Rather than focusing the effort on lightweighting the struts, a greater emphasis could be placed on optimizing the PMM subsystem which accounts for the majority of the mass. The adjustment mechanisms added many additional parts and added significant time, so a different adjustment system such as the differential screws should be reconsidered. Alternative solutions that introduce fewer part counts could simplify manufacturing and assembly. These adjustments might sacrifice some

Primary Mirror Mount:

The primary mirror mount was manufactured from an 18 in x 18 in x 0.625 in plate of Aluminum 6061. The final optimized geometry incorporated rounded corners, circular cutouts, and a large central opening to reduce mass while maintaining structural stiffness. Due to manufacturing complexity and project time constraints, Bill Mildenberger fabricated the base plate and the mounting blocks for the primary optic. The base plate was machined using a CNC milling process.

Following machining, twenty-four 0.5-inch steel balls, serving as mounting legs for the wedge system, were press fit into both sides of the PMM. Dowel pins for the optical mounting blocks were also press fit and used to align and secure the mounting blocks to the base plate.

The twelve wedges used for the adjustment mechanism were similarly fabricated from Aluminum 6061. To meet time constraints, they were CNC machined on a HAAS mill after being cut to a width of 1.5 in on a manual mill. Threads for the thumbscrews were manually tapped to a 10-32 specification. Each wedge includes a 0.75-inch steel ball, which interfaces with the magnetic strut and is installed via press fitting. To maintain positioning, wedges were arranged in mirrored pairs on either side of the plate and connected by springs. These springs apply a constant tensile force, holding the wedges securely in place while allowing controlled adjustment. The manufacturing process of the primary mirror mount can be visualized in Appendix C, figures 27-28.

Secondary Mirror Mount:

The primary material used to manufacture the secondary mirror mount was Aluminum 6061. This material was chosen due to its high stiffness, low mass, and thermal stability. Whilst other materials such as invar provide near zero thermal expansion, preventing misalignment of the secondary mirror. Aluminum provides a more cost-effective solution that carries perks of high thermal conductivity, radiation shielding properties, and simplistic manufacturing processes. Given that tolerances are already meeting specifications, they are consistent with the result from Equation 2. To provide a continuous grain structure and avoid significant material weakness. The mirror mount is CNC machined using a solid block of aluminum on a mill, allowing for tighter tolerances and minimizing structural stresses. The secondary mirror mount consists of 3 separate components. This includes 3-pronged arms that are connected to 2 parallel plates with pin slot - pin holes. At the ends of the spider arms include a slot which also connects to pin slot - pin holes held down with fasteners. The pin slot pin holes were then pressed with dowl pins on each leg starting from the plates outward. In addition, the 0.375-inch balls were then pressed to fit onto the ends of the secondary mirror mount. The fully manufactured secondary mirror mount can be referenced below in the full Cassegrain telescope assembly (Figures 7, 31, 32).

Struts:

The long struts were fabricated from Al 6061 tube stock (OD: .625”, ID: .555”, thickness: .035:”). The manufacturing approach prioritized ease of fabrication and time constraints over topological optimization, as well as ready-made geometry to cut down any additional manufacturing time. The lightweighting of each of the longer struts connecting the PMM and SMM were achieved by drilling 0.375” through holes alternating every 90° along the strut axis at 0.5” spacing, as shown in the final assembly, Figure 32. Hole diameter was constrained to 0.375”, as larger diameter holes produced structural crumpling during the drilling operation. This approach was selected over additive manufacturing due to familiarity with Al 6061 relative to additively manufactured aluminum, as well as the reduced lead time and cost associated with conventional subtractive machining. The short struts connecting the PMM to the camera mounts followed the same manufacturing rationale as the long struts, with through-holes reduced to 0.25 in. diameter to account for the reduced geometry. However, there is also a difference in the spacing of the holes. The lead hole of the patterns is 1 inch from the top of the tube, with a linear pattern of 4 holes with .5” spacing. The holes on the alternate 90° start the linear pattern .25” from the center of the previous holes, as seen in Figures 31 and 32.

Camera Mount:

The camera mount was machined from quarter inch thick aluminum sheet stock. The optimized geometry, which can be seen best in the top image in figure 8, was cut from the aluminum stock using a CNC machine. Steel 0.75” balls were then pressed into the base plate using risers to set the push depth. This process is pictured in figure 31. Finally, in order to mount the raspberry pi mount to the base plate, two holes were drilled and tapped on the side of the plate. This additional feature allowed for a perpendicularly oriented sheet metal piece bent 90 degrees to be fastened to the side with the raspberry pi mounted onto it as seen best in the bottom image of figure 8.

The kinematic mount was machined from aluminum stock using a CNC machine (the design for which can be seen in figure 9). Due to interference between the mount and the base plate, an additional 30 thousandths of an inch were cut from the bottom of the kinematic mount. Magnets were then glued into both kinematic mounts. Additionally, a 3D printed interface part was used to install the camera onto the kinematic mount using 4 standoffs, as pictured in figure 10.

TEST PLAN AND RESULTS

Modal Analysis:

Camera Mount:

The motivation for testing the modes of vibration of the camera mount is governed by our previously defined specification of building a structure with a natural frequency of 180 Hz or higher. The structural natural frequency of the first relevant mode as simulated in Figure 18 was 485.54 Hz. A vibrational test with an accelerometer placet at the point of highest deformation (at the end of one of the flaps) was performed using a hammer. The decrease in frequency between the actual and simulated results can be explained due to the spheres not being modeled in the modal analysis of the part. The spheres should contribute to inertial properties of the larger piece, thus affecting how the system will deform under such a frequency.

Primary Mirror Mount:

The modal analysis for the primary mount was initially simulated in NX with a first relevant mode of 456.336 Hz for the fundamental frequency as shown in Figure 27. When preforming a vibrational hammer test to confirm the simulation results, the fundamental frequency was experimentally determined to be 368.77 hz. This is a lower frequency than the simulation results, which could be due to the additional mass that the physical PMM with the addition of the wedges. Because the fundamental frequency has an inverse relationship with mass, the increase of mass drives the frequency down. This is observed in the experimental results being lower than the simulation. In order to get a more accurate simulation, the weight of the wedges would need to be added if time allowed.

Secondary Mirror Mount:

For the secondary mirror mount, to test the specifications and requirements outlined for this project, a hammer test was done to note the fundamental natural frequencies relative to simulated results. By wiring gauges onto the arms of the secondary mirror mount. Noting that the position Mirrors reflect the point of maximum deflection visualized in the simulations.

Alignment:
Each of the subsystems was created with small deflections in mind. This is why we focused on the stiffness of the PMM, and the lightweighting of the SMM and camera mount. In order to align the optics, a maximum of 0.003 inches would be needed. To confirm that this deflection would be smaller than that maximum value based on our initial measurements as well as our adjustment methods, a laser was used to align the optics as shown in Figure 34.

INTELLECTUAL PROPERTY

The original invention of the classic Cassegrain reflector concept for a telescope was made in 1672 and was accredited to Laurent Cassegrain [4]. However, there have been various patented designs that can involve novel methods of integrating Cassegrain reflection in optical devices, novel methods of alignment, or novel methods of configuring primary and secondary mirrors. Some examples of these are patents FR2886724A, US7595942B2, US5471346A, and CN112230440A. Patent FR2886724A protects a design for a compact Cassegrain telescope device whose primary purpose is position tracking [5]. Patent US7595942B2 protects a design for a light collimating system which can be installed onto a Cassegrain telescope [6]. Patent US5471346A protects a design assigned to Lockheed Martin for a Cassegrain telescope that uses spherical mirror surfaces to minimize distortion for moderate fields of view [7]. Finally, patent CN112230440A protects the design of Sichuan University of an assembly and adjustment mechanism for Cassegrain telescopes as well as the method of assembly and adjustment [8].

Due to the specificity of our Cassegrain telescope design and its relatively small range of applicability, it is possible that our design could be patented. The novelty and non-obviousness of our design are the primary traits that warrant the possibility of a patent. It is most likely that if anything were able to be patented, it would be the mirror supports or adjustment mechanism, which are the parts that were least influenced by existing applications. Since the overall configuration of the optics we used is standard for a Cassegrain telescope, our capabilities to patent this design are restricted to components of the assembly.

SOCIETAL AND ENVIRONMENTAL IMPLICATIONS

Satellite systems, such as the Cassegrain telescope, have a wide impact on many different aspects of our world, from observation of both space and Earth, weather monitoring, global communication, and beyond. Real world satellites provide critical data as well as images that we wouldn't be able to receive any other way. From a global and societal perspective, more advanced satellite data would improve our understanding of our world but also improve connectivity.

This specific project allows for a lower cost way to study optical alignment, structural stability, manufacturing methods, and vibrational effects in space. Less material, time and human resources went into refining our small-scale optical satellite, allowing for a more efficient and accessible approach to understanding and improving challenges that were faced. By understanding what challenges need to be solved and coming up with solutions, it ultimately will allow an easier transition to refine and manufacture a full-scale model.

When looking at the environmental implications of the satellite, the main plates (PMM, SMM, and camera mount) were made from larger pieces of aluminum stock, resulting in excess material that is not easily repurposed for other applications. Additionally, the use of RTV adhesive to secure magnets, along with the various press fit assembly methods, makes recycling or full disassembly very difficult.

RECOMMENDATIONS FOR FUTURE WORK

If given the opportunity for more time for this project, the approach to the SMM design would fundamentally change and how this would affect how the struts design around it. It is a fundamental problem with the stiffness of the structure that significant deflection is seen in the assembly for solution 103 results of the assembly (Figure 21). The approach to strut design would have to account for the lack of stiffness of the SMM by increasing the thickness of the struts. This would increase the area moment of inertia and directly raise the stiffness of the structure. Alternatively, shorter members can and should be used in the future to increase the stiffness of the structure. The strut angle from the SMM to the PMM can also be further optimized, with the SMM having a tighter radius to facilitate a better angle. With the approach to the design of the SMM, the SMM fundamentally acts as a cantilever beam when receiving load and ultimately rocks the structure as it vibrates. A focus moving forward is taking a design approach that provides more robust connection points to the rest of the structure as well as creating opportunities to reduce obstruction of the imaging capabilities. Topology optimization should also be considered for future work for the optimization of the geometry of the PMM and camera mounts. Although their weight is not driving the optimization of the system, there is still the opportunity to remove mass, when possible, as well as decreasing stress concentrations across the individual subsystems.

There was success with the magnet as an interface, but there was uncertainty about how much strength was needed to ensure the best connection or interface. A more thorough analysis and design phase would be needed to solidify this design feature.

Further theoretical optimization of geometry was done on the longer struts, as they stand to benefit most from future optimization. The objective of the theoretical optimization was to minimize mass while maintaining structural integrity under a 1 lbf axial buckling load case, as it scales linearly. Three design iterations were evaluated Iteration A (triangular pattern), Iteration B (four-hole 90° pattern), and Iteration C (helical pattern), and compared to the current manufacturable case. Figure Y shows the 3 design possibilities for future work and their 1st buckling mode (Figure 13).

TABLE 6: Long Strut Design Summary

Design Iteration	Mass [lbm]	Mass Reduction [lbm]	Mass Reduction [%]	1st Mode [psi]	Manufacturable?
Baseline	0.1186	—	—	—	Yes
A	0.0750	0.0436	36.8%	170.54	Yes
B	0.0572	0.0614	51.8%	77.85	Further work is required
C	0.0820	0.0366	30.9%	190.38	Yes

Iteration A employed a triangular offset pattern of 0.4 in. diameter holes at a 1 in. linear spacing along the strut axis. This configuration achieved a mass of 0.0750 lbm and a first buckling mode of 170.54 psi, representing a structurally stable result, with room for improvement. However, the width between adjacent holes approaches a critical minimum threshold, raising concern regarding local buckling at crucial portions of the tube and potential tearing of the inter-hole wall section during both manufacturing and operational loading. While the triangular offset pattern theoretically provides favorable stress distribution. It is certainly possible that the given result is limited by the finite element methods used, more specifically creating a midsurface to simplify the model. A solid body analysis would create more definite results, but computation time is a significant factor to be mindful of. Additionally, further mass reduction through hole enlargement or tighter axial spacing is not recommended without this verification first, as the current geometry is assessed to be near its limit. This is specifically for the current geometry; however, if thicker walled tubes are considered, it opens the opportunity for greater optimization.

Iteration B focused on as large of a reduction in mass as possible. It used a four-hole radial pattern at 90° increments with a 15° axial offset, utilizing 0.375 in. diameter through-holes. This iteration achieved the lowest mass at 0.0572 lbm; however, the corresponding first buckling mode of 77.85 psi represents a significant reduction relative to the other iterations. Iteration B also has the same manufacturability concerns as iteration A. Furthermore, the FEA mesh geometry in regions between holes was flagged as extremely thin, which introduces the risk of artificially high stress results due to poor element quality in those regions. A convergence study is required before the buckling result of this iteration can be implemented in a manufactured design of confidence. Additionally, the offset of the patterned holes creates challenges during manual manufacturing and thus requires a 4 axis CNC to be properly made (if the given length of the strut fits in the machine). The complications needed to pursue such a design create more problems than necessary to pursue such a great reduction in mass. For this optimization to be pursued in the future, stricter and more defined wall geometry should be verified and selected to create better tool path geometry, as well as using standard drill size for the holes. Stiffness is also a concern, and thicker tube walls should be pursued if this design is used in the future.

Iteration C employed a helical hole pattern using a 27/64” diameter drill size, selected to correspond to available tooling. The helical pattern was experimented with the idea in mind that torsion could occur under significant gravity loads and a helical pattern could compensate for such possibilities. If larger holes are used with the following pattern, the pattern fails to generate/create intersecting holes. The helix was defined with an angle of 90°, a pitch of 1.75”, and 10 turns, with 2 holes oriented 0.5” apart that the pattern was made from. from the WCS origin. This configuration achieved the highest first buckling mode at 190.38 psi, with a mass of 0.0820 lbm, demonstrating that the helical distribution of material removal provides a more favorable buckling response relative to Iterations A and B. Manufacturability was assessed as achievable; however, the helical pattern requires either a 4 axis CNC, or precise manual indexing, both of which introduce unnecessary alignment error and increased setup time. It should be noted that additional space exists within the current helix geometry to introduce a second helical pattern, which could reduce mass further while potentially maintaining or improving buckling performance through more uniform hole distribution. This double-helix variant represents the most promising avenue for future optimization.

Of the three iterations explored for the long struts, iteration A and C hold the most promise for application to the short struts. A's hole spacing could be downscaled by reducing the hole diameter below the current 0.4 in. and tightening the axial spacing to accommodate the ~2.8 in. strut length; spacing between holes would need to be monitored carefully. Iteration C's helix pattern would require complete re-parameterization, specifically a reduced pitch and fewer turns, to produce a viable pattern within the constrained geometry. Iteration B should not be considered, as the four-hole 90° radial pattern at the current hole sizing leaves minimal ligament width even on the longer strut, and scaling the hole size to the shorter geometry is likely to compromise structural integrity. The modal analysis of the struts should be considered at the assembly level. As seen with the results of the analysis of the assembly. Although the struts can be theoretically stiff, major deformation or displacement can occur at lower frequencies.

From the modeling perspective, a more in-depth model in the future should be considered that takes into account not only the preloading of all bolts, dowels, and the magnets, but the compensation of the kinematic mounting for the main structures. The thermal analysis as well can be deemed less than perfect. A dedicated physical thermal analysis as well as a more in-depth 101 solution that accounts for the dissimilar materials at the interface and internal to the structure (i.e. the magnets, circuitry, expansion of any bolt connections or dowels). There also should be a general approach to mesh refinement and specificity in modeling approach.

ACKNOWLEDGMENTS

The team would like to thank Dr. Chris Muir for being our sponsor for this project, providing support and guidance through the design and manufacturing process. An additional sincere thank you is warranted to Bill Mildenberger, Chris Pratt, Sam Kriegsman, Angel Bermudez, and Jim Alkins for their assistance and support during this project as well as their flexibility and availability when assisting.

REFERENCES

[1] R. G. Budynas, J Keith Nisbett, and Joseph Edward Shigley, *Shigley's mechanical engineering design*, 11th ed. New York, Ny: Mcgraw-Hill Education, 2020.

[2] Siemens Digital Industries Software, NX Material Library, NX 2506, 2025. Accessed: Apr. 26, 2026. [Online]. Available: https://www.plm.automation.siemens.com/

[3] K. S. NIAKI, A. ANVARI, and F. FARHANI, "Aluminum and composite materials for satellite structures A comparison of thermal performance," Materials Science Research india, vol. 4, no. 1, pp. 25–34, Apr. 2007, Accessed: Apr. 26, 2026. [Online]. Available: https://materialsciencejournal.org/pdf/vol4no1/MSRIVol04N1P25-34.pdf

[4] Baranne, André; Launay, Françoise (1997). "Cassegrain: un célèbre inconnu de l'astronomie instrumentale" [Cassegrain: a famous unknown of instrumental astronomy]. Journal of Optics (in French). 28 (4): 158–172. doi:10.1088/0150-536X/28/4/004.

[5] Didier Godart, et al. *Compact, Lightweight Central Position Guiding Plant, e.g. for Orbiting Missile or Spacecraft, Includes Core Structure with Accelerometer(s), Gyroscope(s), Mirrors and Cassegrain Telescope as Star Viewer*. 8 Dec. 2006.

[6] Koenig, Dean B. *Light Collimating System for Schmidt-Cassegrain Telescope*. 29 Sept. 2009.

[7] Ames, Alan J. *Casegrain Telescope with Spherical Mirror Surfaces*. 28 Nov. 1995.

[8] *Cassegrain Telescope Assembling and Adjusting Mechanism and Assembling and Adjusting Method*. 28 Dec. 2021.

[9] R. G. Budynas and J. K. Nisbett, *Shigley's Mechanical Engineering Design*, 11th ed. New York, NY, USA: McGraw-Hill Education, 2019.

APPENDIX A (CAD/DESIGN):

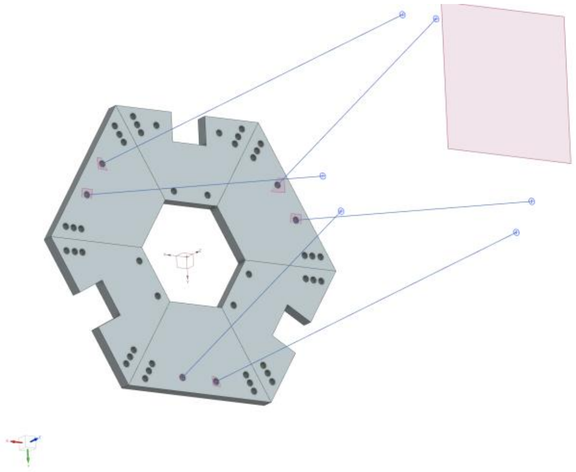

Figure 1: 6 trapezoidal Primary Mirror mount concept which includes interface area with both the camera struts and the SMM struts

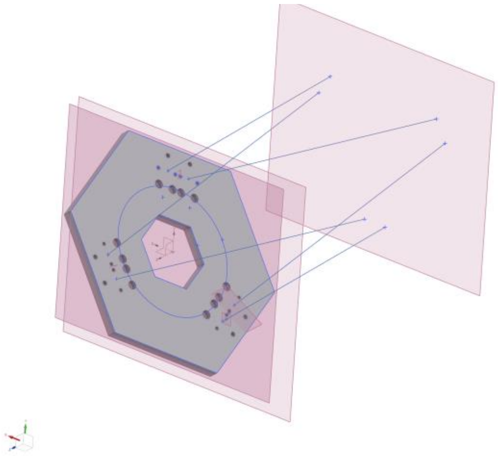

Figure 2: Single hexagon plate concept for PMM which was the selected concept for plate before lightweighting.

Figure 3: An example mechanical ball and socket joint

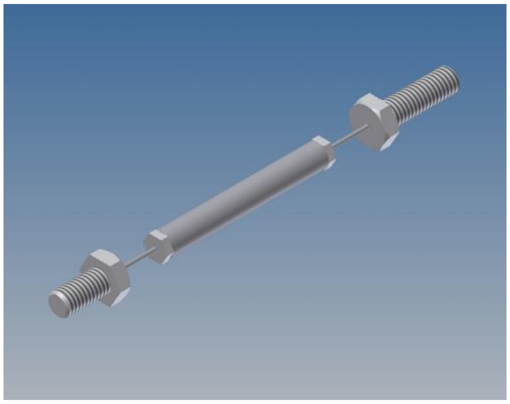

Figure 4: An example mechanical wire flexure and rod joint system

Figure 5: An example magnetic rod and steel ball attachment mechanism

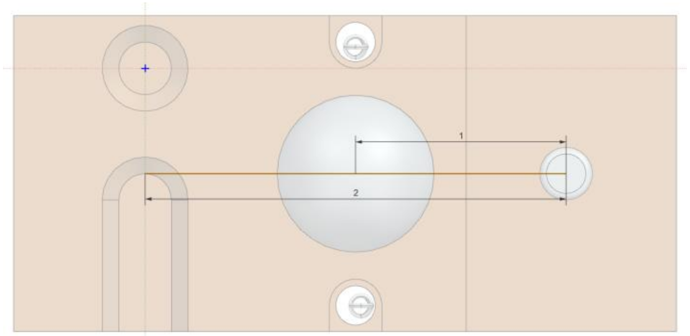

Figure 6: distances between thumbscrew and rotation point (2”) and between thumbscrew and strut base (1”). View shown is from the bottom of the adjustment wedge.

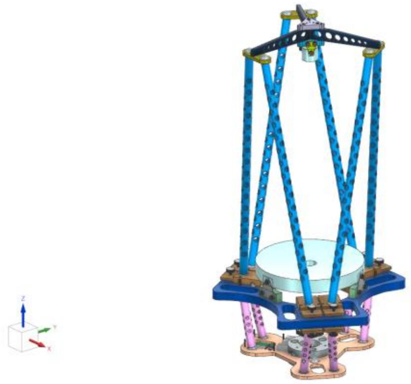

Figure 7: Trimetric view of final CAD.

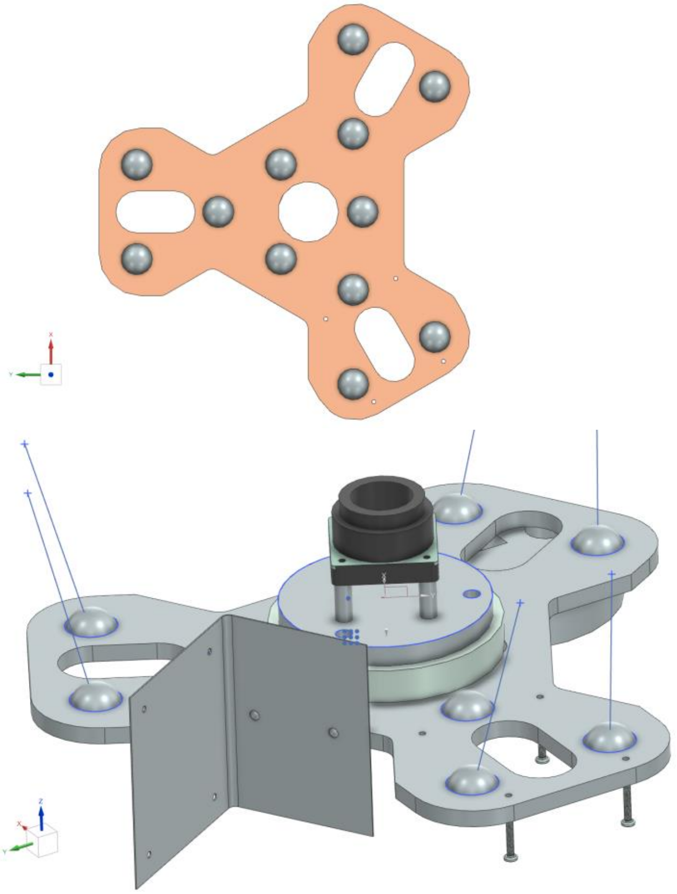

Figure 8: top view of lightweighted camera mount base plate, spherical steel balls pressed into holes, the bottom image features the installed camera and kinematic mount as well as the perpendicularly installed pi mount.

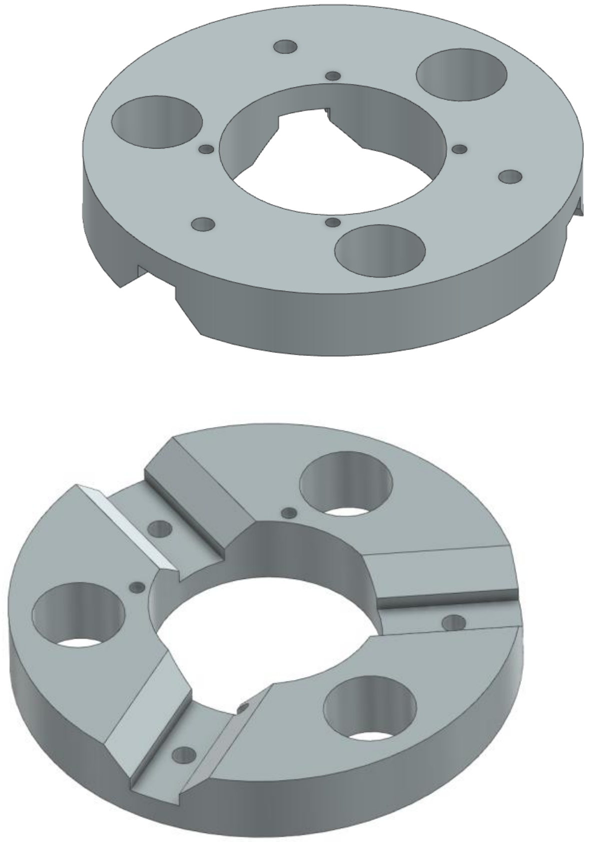

Figure 9: Kinematic mount design for camera. 3 vees provide contact with three steel balls. Holes through the flats in each vee allow for magnet installation.

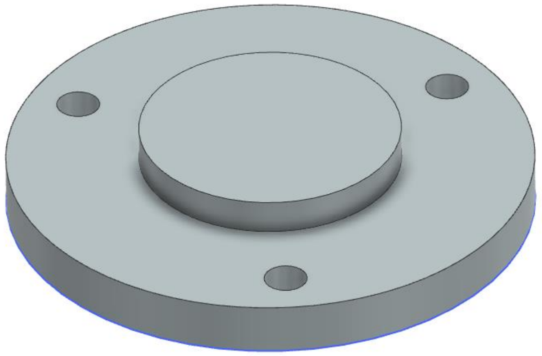

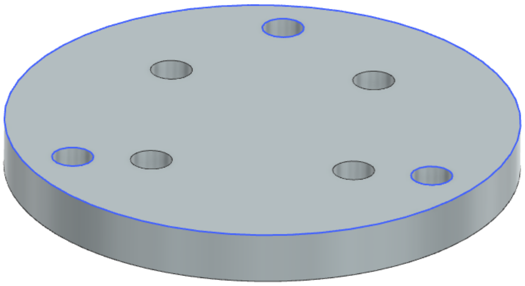

Figure 10: Interface between camera and kinematic mount. The three holes visible in the top picture allow for installation of steel pins which hold the interface to the magnets in the kinematic mount. The four central holes in the second picture allow for the pressing in of 4 standoffs, to which the camera is fastened.

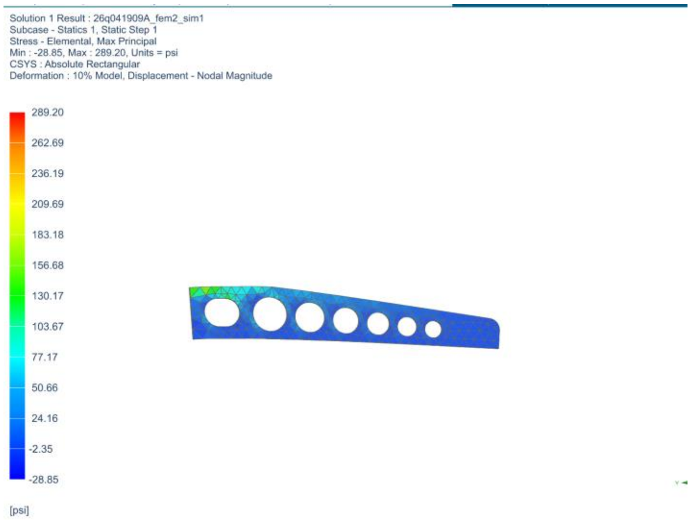

```
Solution 1 Result : 26q041909A_fem2_sim1
Subcase - Statics 1, Static Step 1
Stress - Elemental, Max Principal
Min : -28.85, Max : 289.20, Units = psi
CSYS : Absolute Rectangular
Deformation : 10% Model, Displacement - Nodal Magnitude
```

Figure 10: Secondary mirror mount with holes subjected to 18G’s of force.

APPENDIX B (SIMULATION AND TESTING):

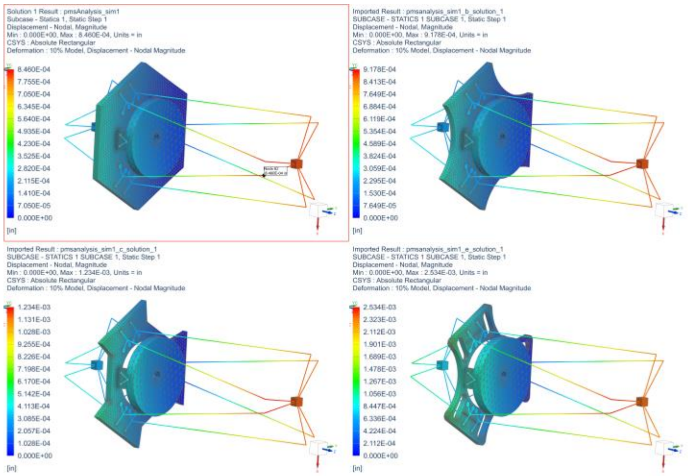

Figure 11: Structural FEA iterations of the Primary Mirror Mount starting with the baseline (A) in the upper left, B in upper right, C, in lower left and the final (D).

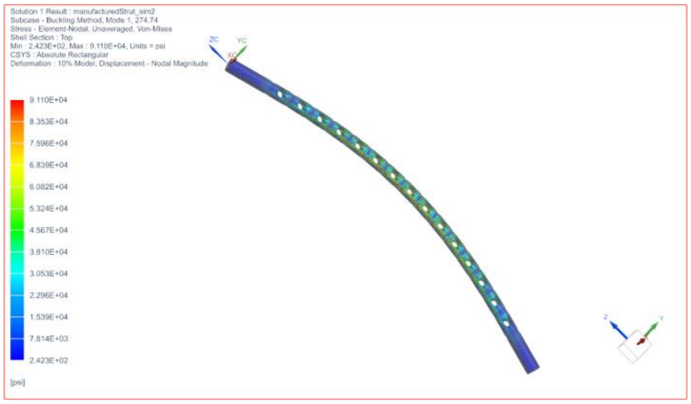

Figure 12: FEA Simulation of longer struts. Stress-Element-Nodal results of manufactured strut. RBE2's were used at either edge simulating the ball joint. SPC12 is present at the top and SPC1236 is at the bottom. Solution 105, CQUAD4 (.15 in mesh), Al 6061 (NX Library). FOS determined to be 274.74 psi under 1 lbf axially.

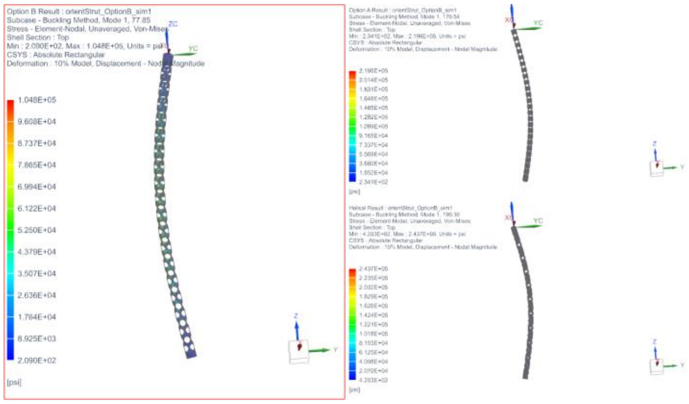

Figure 13: FEA Simulation Stress-Element-Nodal results of theoretical optimized strut. Solution 105, CQUAD4 (.15 in mesh), Al 6061 (NX library). Iteration B produced the best reduction in mass and hence possible reduction of FOS closer to proposed specification.

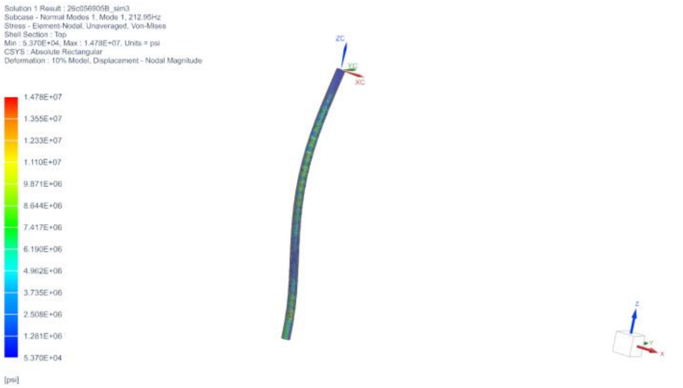

Figure 14: Modal results (Solution 103) of the longer struts. RBE2's were used at either edge simulating the ball joint. SPC12 is present at the top and SPC1236 is at the bottom. CQUAD4, .1" mesh size, Al-6061 (NX Library). First mode of 212.95 Hz

Figure 15: FEA Simulation of shorter struts. Stress-Element-Nodal results of manufactured strut. Solution 105, CQUAD4 (.0833 in mesh), Al 6061 (NX Library). FOS determined to be 1.076E4 psi under 1 lbf axially. Same boundary conditions and constraints present as Figure 14.

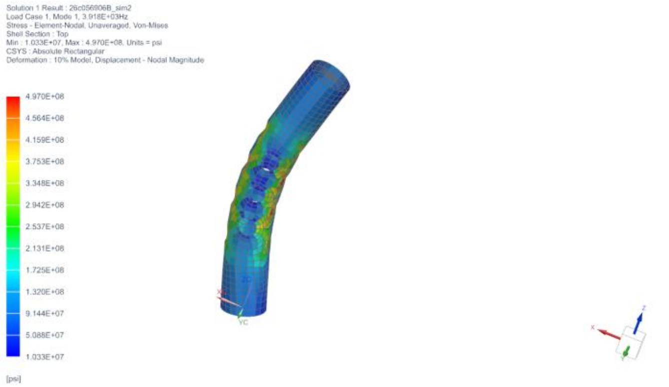

Figure 16: Modal results (Solution 103) of the shorter struts. RBE2 was used at either edge simulating the ball joint. SPC12 is present at the top and SPC1236 at the bottom. CQUAD4, .0.0833” mesh size, Al-6061 (NX Library). First mode of 3.918E3 Hz.

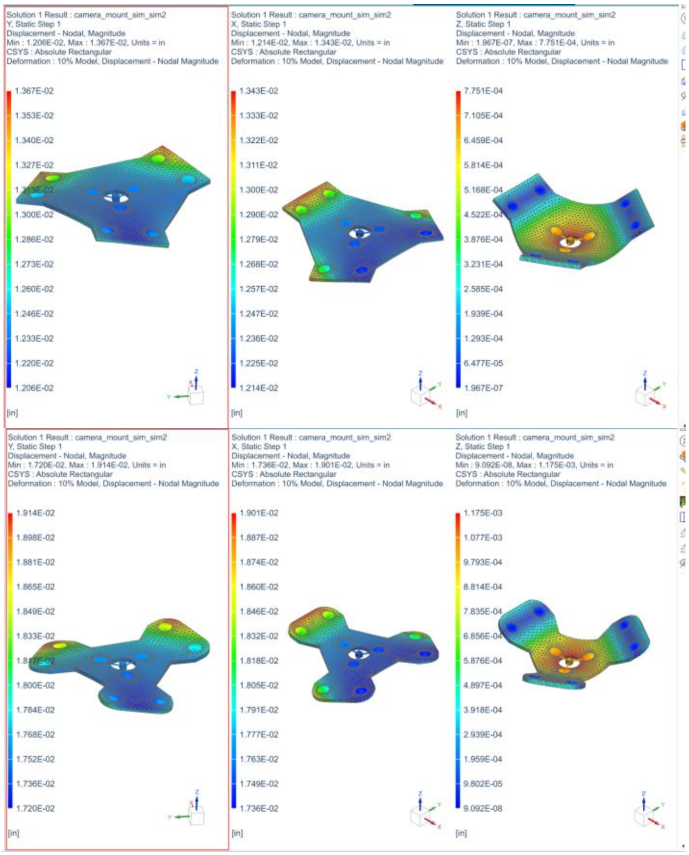

Iteration	Weight (lbf)	Maximum Deformation (in)
1	1.3323	1.37E-02
2	1.0127	1.91E-02
3	0.8433	2.08E-02

Figure 17: Lightweighting process of the camera mount depicting the deformation when the gravitational load is applied in the X, Y, and Z directions. The table below shows the maximum deformation and weight values corresponding to each design iteration.

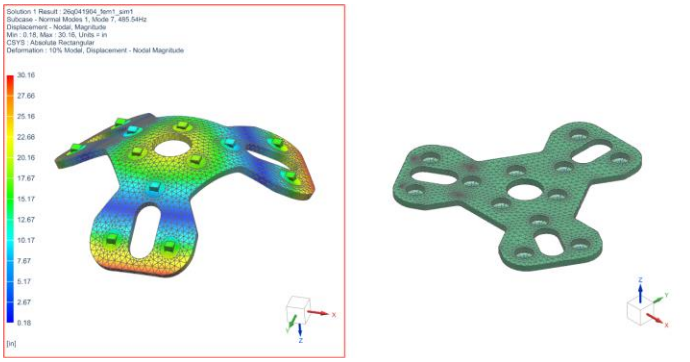

Figure 18: Modal FEA analysis results for the camera mount. The simulation used a 103 type solution as well as an element type of Tet10 (.25in in size), and an assigned material of NX Aluminum 6061.

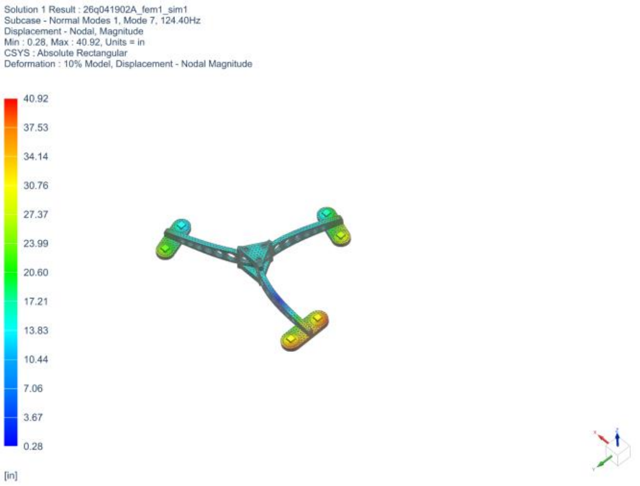

Figure 19: SOL 103 Real eigenvalue analysis, displacement results for the secondary mirror mount utilizing CQUAD10 elements. Al-6061 used as material


Solution 2 Result : 26q041902A_fem1_sim1
Subcase - Statics 1, Static Step 1
Displacement - Nodal, Magnitude
Min : 0.000E+00, Max : 8.829E-06, Units = in
CSYS : Absolute Rectangular
Deformation : 10% Model, Displacement - Nodal Magnitude

Figure 20: SOL 101 statics NX displacement results, for objects meshed using CQUAD 10 elements. Al-6061 used as the material.


Solution 1 Result : 26q041900A_sim2
Subcase - Normal Modes 1, Mode 7, 112.30Hz
Displacement - Nodal, Magnitude
Min : 0.07, Max : 31.94, Units = in
CSYS : Absolute Rectangular
Deformation : 10% Model, Displacement - Nodal Magnitude

Figure 21: Displacement results from the modal analysis of the assembly in the absolute deformation case. The SMM is seen causing the rest of the assembly to deform. SOL 103, Al 6061, CTETRA(10), mesh sizes of .3” and .7” present. Max displacement 31.94” from 112.3 Hz.

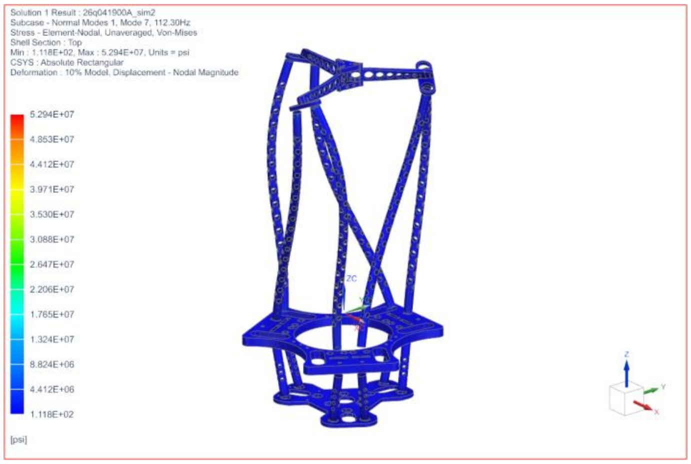
Solution 1 Result : 26q041900A_sim2
Subcase - Normal Modes 1, Mode 7, 112.30Hz
Stress - Element-Nodal, Unaveraged, Von-Mises
Shell Section : Top
Min : 1.118E+02, Max : 5.294E+07, Units = psi
CSYS : Absolute Rectangular
Deformation : 10% Model, Displacement - Nodal Magnitude

Figure 22: Stress Results from the solution 103 of the assembly. Max stress is low with Strain energy results correlating results in Figure YY. Al 6061, CTETRA(10), mesh sizes of .3” and .7” present.


Solution 1 Result : 26q041900A_sim2
Subcase - Normal Modes 1, Mode 7, 112.30Hz
Strain Energy Density - Elemental, Scalar
Min : 2.028E+02, Max : 1.433E+07, Units = lbf·in/in³
Deformation : 10% Model, Displacement - Nodal Magnitude

Figure 23: Strain energy density of the assembly from the first mode. SOL 103, Al 6061, CTETRA(10), mesh sizes of .3” and .7” present.

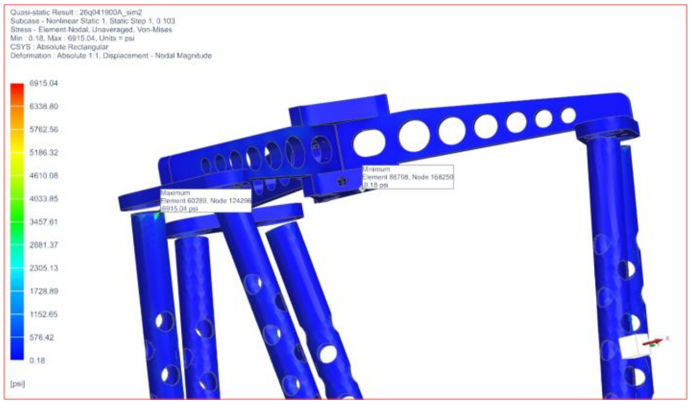
Quasi-static Result : 26q041900A_sim2
Subcase - Nonlinear Static 1, Static Step 1, 0.103
Stress - Element-Nodal, Unaveraged, Von-Mises
Min : 0.18, Max : 6915.04, Units = psi
CSYS : Absolute Rectangular
Deformation : Absolute 1:1, Displacement - Nodal Magnitude

Maximum
Element 60289, Node 124296
6915.04 psi

Minimum
Element 88708, Node 168250
0.18 psi

Figure 24: 18g element nodal result. Stress concentration at the RBE2 connection points. Results present indicate some level of

artifacting. SOL 106, Al 6061, CTETRA(10), mesh sizes of .3” and .7” present.

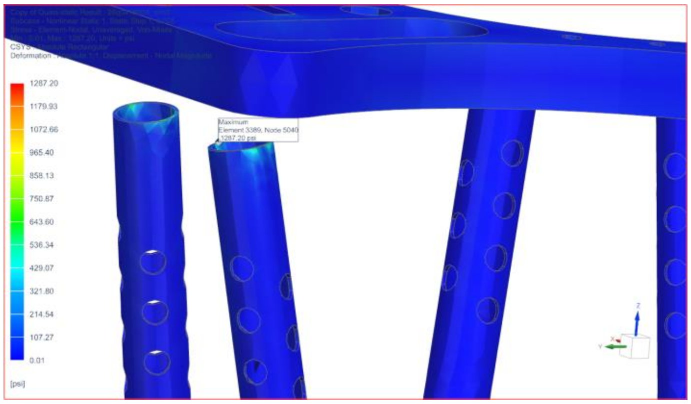

Figure 25: 12g element nodal result. Stress concentration at the RBE2 connection points. Results present indicate some level of artifacting. SOL 106, Al 6061, CTETRA(10), mesh sizes of .3” and .7” present.

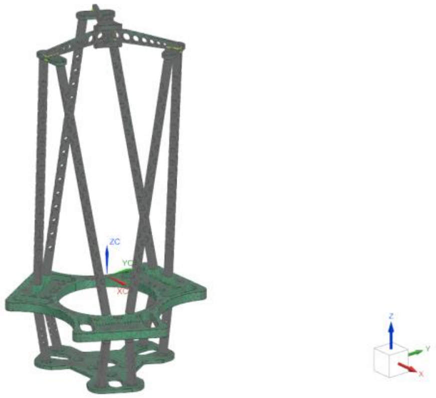

Figure 26: Mesh of the assumed geometry of the assembly model. CTETRA10 elements were used throughout. RBE2 spider connections were used to simulate the ball joints, although adding artificial stiffness to the system. Mesh sizes were .3” for the main structural elements and .7” for the PMM and camera mount

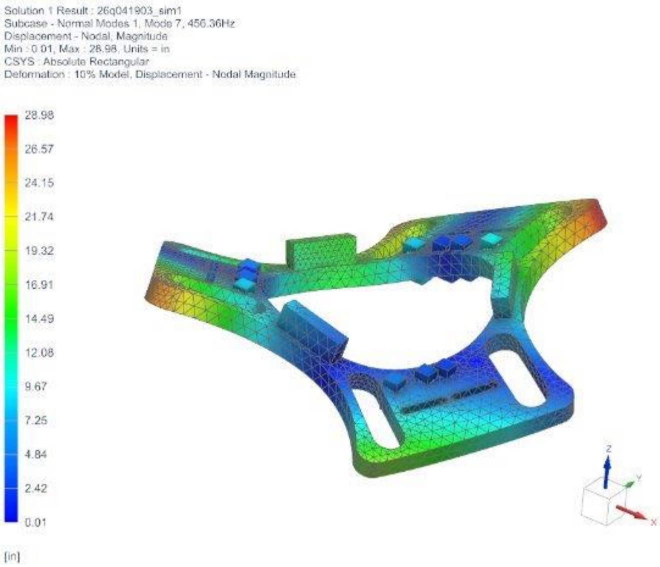
Solution 1 Result : 26q041903_sim1
Subcase - Normal Modes 1, Mode 7, 456.36Hz
Displacement - Nodal, Magnitude
Min : 0.01, Max : 28.98, Units = in
CSYS : Absolute Rectangular
Deformation : 10% Model, Displacement - Nodal Magnitude

Figure 27: Modal simulation of PMM with a first relevant frequency of 456.336 Hz

APPENDIX C (MANUFACTURING):

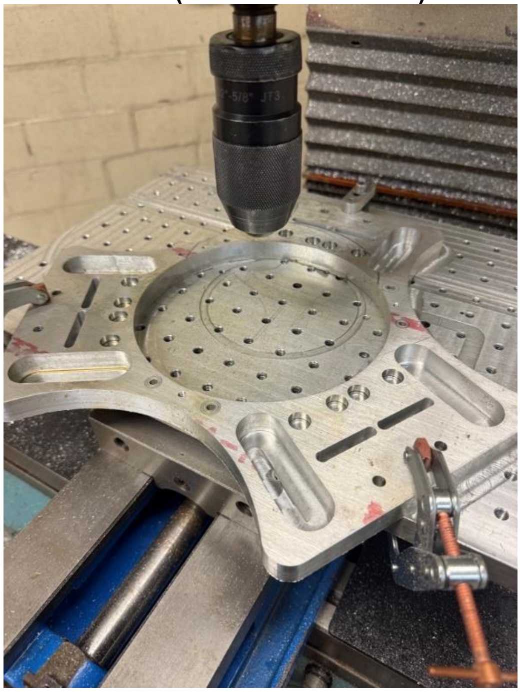

Figure 28: Primary Mirror Mount after being initially cut to size and optimized.

Figure 29: Primary Mirror mount with the press fit balls, and the adjustment wedges and partial optical mounting blocks installed.

Figure 30: Close up view of the strut connecting the PMM and camera mount. Final lightweight design.

Figure 31: Press fit process of steel balls into camera mount

Figure 32: Final assembly on satellite mount. Matches fixed constraint present in assembly simulation. Light weighted struts can be seen in the center of the frame along with the PMM and SMM.

Figure 33: Final assembly of the satellite. Clearer view of optical path and the SMM. The camera and its kinematic mount can be seen on the right side of the image.

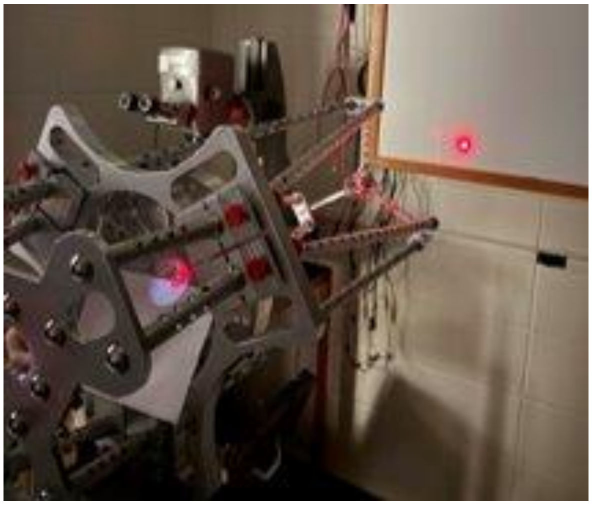

Figure 34: Using laser to align the optics